Colloids and Surfaces A: Physicochemical and Engineering Aspects 698 (2024) 134524

Contents lists available at ScienceDirect

Colloids and Surfaces A: Physicochemical and Engineering Aspects

journal homepage: www.elsevier.com/locate/colsurfa

A facile method to obtain colloidal dispersions of nickel hydroxide: Improving the processing of nickel oxide and facilitating its upscaling for perovskite-type solar devices

Rafael Martí Valls [a,*], Rodrigo García Rodríguez [a,b], Diana Meza Rojas [c], Tom Dunlop [a], Eurig Jones [b], Suzanne K. Thomas [a], Matthew L. Davies [a,d], Peter J. Holliman [c], Jenny Baker [a], Cecile Charbonneau [a,e]

[a] SPECIFIC, Faculty of Science and Engineering, Swansea University, Bay Campus, Swansea SA1 8EN, UK
[b] IMPACT, Faculty of Science and Engineering, Swansea University, Bay Campus, Swansea SA1 8EN, UK
[c] CEMEG, Faculty of Science and Engineering, Swansea University, Bay Campus, Swansea SA1 8EN, UK
[d] School of Chemistry and Physics, University of KwaZulu-Natal, Durban, South Africa
[e] Ceres Power Ltd, Foundry Lane, Viking House, Horsham RH13 5PX, UK

GRAPHICAL ABSTRACT

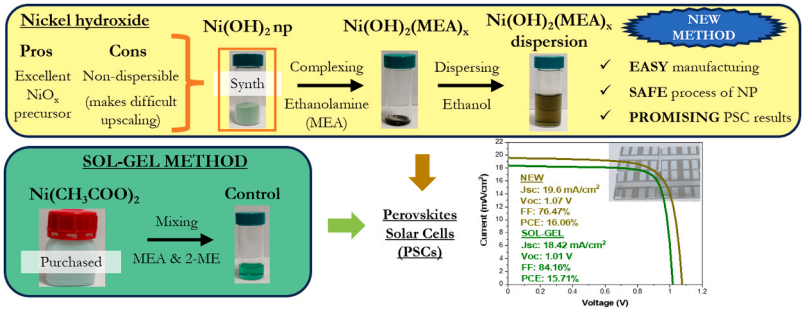

ARTICLE INFO

Keywords:
Nickel hydroxide
Nickel oxide
Semiconductor processing
Nanoparticle dispersion
Perovskite solar cells

ABSTRACT

Nickel hydroxide has been successfully employed as a precursor to the widely used, inorganic hole transport material (HTM) nickel oxide (NiO_x). However, manufacturing NiO_x HTM layers from nickel hydroxide is more complicated than those involving organometallic precursors due to its poor solubility/dispersibility. We report here a substantial increase in nickel hydroxide dispersibility in organic solvents by complexing it with mono-ethanolamine. These improvements have enabled us to develop a simpler method for processing nickel hydroxide that resemble the known sol-gel method. The new metal complex remains dispersed for months and converts to nickel oxide at a temperature similar to that of nickel hydroxide (270–300 °C). An extensive characterisation of NiO_x films obtained from the deposited precursor has been carried out. Perovskites solar cells have also been built with these films as a proof of concept, showing promising results for the layers sintered at low (270 °C) and high (500 °C) temperatures. The pixel with highest efficiency for both sintering temperatures were 14.7 % and 16.7 %, respectively, which are close to or surpass the ones of the control samples (15.4 % and 15.7 %,

* Corresponding author.
E-mail address: r.f.martivalls@swansea.ac.uk (R. Martí Valls).

https://doi.org/10.1016/j.colsurfa.2024.134524
Received 8 April 2024; Received in revised form 31 May 2024; Accepted 11 June 2024
Available online 12 June 2024

respectively). The applied unpaired t-test statistical method showed that the mean efficiency values for our thick samples prepared at 270 °C are not statistically different from those of the control cells. Furthermore, the samples prepared at 500 °C presented a significant statistical difference with the control cells, showing higher average efficiencies (12.8 % and 13.3 % versus 11.4 % and 11.7 %, reverse and forward measurements, respectively). The simplicity of the manufacturing method developed, together with the use of non-toxic organic compounds for its preparation and the promising results observed in solar devices, makes it suitable for being upscaled.

1. Introduction

Thanks to its unique combination of properties, nickel oxide has been used in a large number of fields, such as batteries[1], gas sensors[2], antimicrobial[3] and electrochromic[4] materials, catalysts[5], optical filters[6], ceramic structures[7,8], cements[9], efficient smart windows [10] and photovoltaics[11,12], but particularly perovskites solar cells (PSC)[11,13–15] and organic solar cells[16,17]. PSC devices use nickel oxide (NiO_x) as a hole transport material (HTM) due to its p-type conductivity and an energetically favourable energy level alignment with photoactive lead halide perovskite-type absorbers [11]. It is often preferred to other HTM candidates such as spiro-OMeTAD[15,18], PEDOT:PSS[17], poly-TPD[19], PTAA[18], V_2O_5[20], $CuInS_2$[21], CuSCN[22] or Cu_2O[23] due to its high optical transmittance in comparison to other inorganic HTM, hole conductivity and long-term chemical stability [11]. Chemical and high vacuum methods to obtain nickel oxide films for PSC have been developed[11,24–29] with the built devices showing promising efficiencies (power conversion efficiencies (PCE) of ca. 19 %)[25,26]. Low-vacuum and non-vacuum methods are preferred due to their easier processing, lower capital costs of equipment and potential to scale. These require close control (e.g., homogeneity and stability of the precursor solution, uniform deposition along the substrate) to achieve consistent HTM layers. As such, various chemical methods have been tested to obtain NiO_x, such as, atomic layer deposition (ALD)[30], solvothermal[31], microwave synthesis[32] and electrodeposition[33]. One of the most widely used is the sol-gel route due to its simplicity[12,24,25,34–36]. This method consists of dissolving a nickel organic salt together with a stabilizing agent in an organic solvent. The resulting solution is later deposited and thermally treated to obtain NiO_x. Several metalorganic precursors have been tested[24,25,37]. These salts decompose to form the metal oxide at different temperatures which limits the substrates which can be used, e.g., nickel formate ($T_{process}$>340 ºC)[38,39], nickel acetate ($T_{process}$>350 ºC)[40], nickel bisacetylacetonate ($T_{process}$= 345 ºC)[41] and nickel oxalate ($T_{process}$= 365 ºC)[42]. In practice, these precursors are calcined at temperatures well above their decomposition temperature to improve device efficiency[25,43] (450–500 ºC). These temperature values also restrict the transparent conducting oxides (TCOs) that can be used to build the devices[44].

Another widely used method is based on the synthesis of nickel oxide nanoparticles (NPs) which generally uses pre-synthetised nickel hydroxide as the NPs precursor. The hydroxide decomposes into oxide NPs at the lowest temperatures reported among NiO_x precursors (i.e., 270 and 300 ºC)[14,15,29,45–47]. Subsequently, the oxide particles obtained are dispersed by sonication and deposited. This method has produced PSC devices with PCE ranging from 15 % to 21 % depending on device configuration[15,29,45,47]. It is also suitable for flexible substrates, since NiO_x is already present and only some heating is necessary to evaporate the remaining solvent (120 ºC)[45]. Furthermore, NP-based films can be tuned through their particle size to adjust their energy level positions. This in turn can improve PSC efficiency due to improved charge extraction[11]. Although this method has several advantages over the sol-gel method, it requires more preparation steps which complicates industrial upscaling. To simplify the process of obtaining NiO_x films from nickel hydroxide, other techniques such as electrochemical deposition[33] can be used. This technique deposits nickel hydroxide directly on the substrate, which gives it better processability than the NPs method and prevents the presence of dangerous nanoparticle dust during the manufacturing process. A PSC device efficiency of 21.74 % after UV ozone (UVO) surface treatment has been reported for these films[33]. Although electrodeposition of nickel hydroxide involves less complexity and is safer than processing the nickel hydroxide in the manner presented above, this method is still far from the simplicity of the sol-gel method. A straightforward method that allows to use nickel hydroxide nanoparticles as a precursor for NiOx films hasn't yet been developed.

In this paper, we present a simple method to manufacture NiO_x films using nickel hydroxide as a precursor. We prepared an organometallic compound from a previously synthesised nickel hydroxide powder and monoethanolamine that is easily and quickly dispersible in ethanol, unlike nickel hydroxide[48]. The obtained colloidal dispersion is very stable, showing no sedimentation several months after preparation. The simplicity of this process is similar to that of the sol-gel method since only hydroxide powder and amine need to be mixed. Furthermore, this method avoids colloidal dispersion by sonication and thermal treatment of the precursor powder in the oven (both steps characteristic of the NPs method) whilst the material retains a decomposition temperature close to that of nickel hydroxide (i.e., best among NiO_x precursors). By removing these steps, we simplify NP processing, making it easier to upscale and combine the smooth processing of the sol-gel method with the advantages of using nickel hydroxide as NiO_x precursor. The obtained nickel oxide films have been electrically, optically, morphologically, and compositionally characterised. Finally, we show its potential application as HTM on inverted PSC devices demonstrating the validity of this method.

2. Experimental section

All chemicals were purchased from Sigma-Aldrich unless stated otherwise. Chemical purities are those provided by suppliers. All samples were prepared using the chemicals from these suppliers and with those purities. All compounds were weighed using an analytical balance (±0.1 mg).

2.1. Synthesis of nickel hydroxide (P1)

Synthesis of this precursor employed the coprecipitation method developed by Fei Jang *et al.*[48]. Briefly, 54.2 mmol of nickel (II) nitrate hexahydrate (99.999 %) was dissolved in 100.0±0.1 mL of distilled water using magnetic stirring. Then 50.0±0.1 mL of a 10 M sodium hydroxide (≥98 %) solution was prepared using a volumetric flask. It was added drop-by-drop to the stirred nickel solution until reaching a pH of 10.00±0.01 (Orion Star a211 pHmeter). The obtained green powder was filtered using Buchner funnel vacuum filtration (Whatman qualitative filter paper, grade 1) and washed with DI water and ethanol. The powder was dried for 6 h at 80 ºC in a conventional oven. Finally, the powder was ground in an alumina mortar.

2.2. Preparation of nickel hydroxide-monoethanolamine complex (M1)

50.0 mg of nickel hydroxide powder (P1) and 2.7 mmol of monoethanolamine ((≥99 %), molar ratio 1:5) were mixed with a stirring bar at 40 ± 5 ºC using a hot plate stirrer. Samples stirred for different times were prepared: 24 h (D_{24h}), 48 h (D_{48h}) and 72 h (D_{72h}).

2.3. Nickel complex dispersion, film deposition, and thermal treatment

The resulting nickel complex was mixed with ethanol (≥ 99.8 %, Fisher Scientific) and shaken for 1 min. The solid content was 1.25 % (weight % of nickel hydroxide precursor; the weight % of the other components was: 4.12 % of monoethanolamine and 94.63 % of ethanol). A turbid dispersion was obtained and filtered with a 0.2μm PTFE filter. The filtered dispersion was deposited on soda lime-glass (SLG) and TEC-7 fluoride-doped tin oxide (FTO) by spin coating at 6000 rpm for 30 s. The films were thermally treated at 180 ºC (F_{180}), 270 ºC (F_{270}), 320 ºC (F_{320}), 400 ºC (F_{400}) and 500 ºC (F_{500}) for 30 min in a high temperature titanium hot plate (±2 °C).

2.4. Solar cell fabrication

Lead iodide (99.99 %) was purchased from TCI Chemicals. [6,6]-Phenyl-C61-butyric acid methyl ester (PCBM) was purchased from Ossila (Sheffield, United Kingdom).

2.4.1. Preparation of substrates

FTO glass was employed as the substrate (2.7×2.7 cm^2). A small strip of the FTO layer (0.5±0.1 cm) was removed by employing zinc powder and a 2 M solution of hydrochloric acid (HCl, prepared with a 20.0 ±0.1 mL volumetric flask). The substrates were rinsed with deionised water and sequentially sonicated in an ultrasonic bath at 40 °C for 15 min with 2 % (vol%) Hellmanex detergent, water, acetone, and isopropanol. The substrates were then dried to N_2 and treated by plasma irradiation (oxygen plasma cleaner) for 8 min prior to the deposition of the device layers.

2.4.2. Preparation of hole transport layers (HTLs)

NiO_x films were prepared on cleaned FTO substrates. The nickel complex dispersion that was developed in this manuscript and a control solution (sol-gel method, nickel acetate dihydrate dissolved in 2-methoxyethanol[43]) were used to obtain these films.

Nickel complex solution films were spin-coated for 30 s at 6000 rpm ("thin" films) and 2000 rpm ("thick" films) and heated in a high temperature titanium hot plate (±2 °C) for 30 min at 270 ºC and 500 ºC. These films were labelled -thin(270), thick(270), thin(500) and thick (500) films. No thickness measurements were made.

Control solution films were spin-coated for 30 s at 3000 rpm[43] and heated in a high temperature titanium hot plate (±2 °C) for 30 min at 270 ºC and 500 ºC. These films were labelled -control(270) and control (500) films-.

Table 1 shows a summary of the samples prepared. Similar films were prepared for the cyclic voltammetry analysis.

Table 1
Description of NiO_x samples prepared for solar devices and cyclic voltammetry analysis.

Sample	Nickel precursor concentration (M)	Spin coater speed (rpm, 30s)	Heating temperature (ºC)	Precursor
Thin (270)	0.11	6000	270	Nickel hydroxide
Thick (270)	0.11	2000	270	Nickel hydroxide
Control (270)	0.20	3000	270	Nickel acetate
Thin (500)	0.11	6000	500	Nickel hydroxide
Thick (500)	0.11	2000	500	Nickel hydroxide
Control (500)	0.20	3000	500	Nickel acetate

2.4.3. Assembly of perovskite solar cell (PSC) devices

All the PSCs were fabricated with the inverted configuration (p-i-n). For the perovskite layer, a 1.25 M solution of methyl ammonium iodide (MAI) and lead iodide (PbI_2) in a 4:1 v/v mixture of dimethyl formamide/ dimethyl sulfoxide (DMF/DMSO) was prepared before filtering through a 0.2 μm PTFE syringe filter. The perovskite solution was spin-coated over the NiO_x-coated substrates at 4000 rpm for 30 s in a N_2-filled glovebox. 200 μL of ethyl acetate were dropped as antisolvent as close to 7 s as possible (looking at stopwatch) after the start of the spin-coating of the perovskite layer. The perovskite films were then placed on top of a high temperature titanium hot plate (±2 °C) at 100 °C for 10 min and left to cool down for two additional minutes. 100 μL of a 22 mM solution of PCBM in chlorobenzene was spin coated on top of the perovskite layer at 3000 rpm for 30 s and allowed to dry. Finally, 100 μL of a 1.4 mM solution of bathocuproine (BCP) in ethanol was spin coated on top of the PCBM layer at 6000 rpm for 30 seconds and allowed to dry. Silver was evaporated as the metallic contact in a high-vacuum physical vapour deposition chamber (Edwards E306 Bell Jar Evaporator) under pressure below 1.5 $\times 10^{-5}$ mbar. Each substrate had 8 pixels per substrate.

2.5. Characterisation

The crystallinity of the powders and films was analysed by X-Ray Diffraction (Bruker D8 Discover XRD) using Cu K_α radiation source (λ = 1.5406 Å, angle range $2\theta = 30-85$). Thermogravimetric Analysis and Differential Scanning Calorimetry in air (TGA/DSC) was used to find the hydroxide to oxide transition temperature of the precursor powder (STA6000, Perkin Elmer) and to analyse the thermal chemistry of the metallic complex (Seteram Labsys Evo (STA)). Pyrolysis-gas chromatography-mass spectrometry (Py-GC-MS, Pyrolizer: CDS Analytical Pyroprobe 5000 series, GC: Agilent 7890B and MS: Leeco Pegasus BT) and Fourier transform infrared spectroscopy (FTIR Microscope, Perkin Elmer Spotlight 400) were used to analyse the functional group in the precursors. The Tyndall effect of the dispersions was imaged with a Canon EOS 750D camera (exposure time: 13 s, camera aperture: F5.6, ISO sensitivity: 400) using a red laser (630–680 nm wavelength) as light source. UV/visible spectroscopy (Perkin Elmer Lambda 9 UV-Vis-NIR spectrometer) was used to obtain transmission spectra of nickel oxide films and FTO substrate (wavelength range λ = 300–800 nm). The films wettability was analysed by contact angle (FTA 1000 B Class) using distilled water. The morphology of nickel hydroxide precursor powder was analysed by scanning electron microscopy (SEM, JEOL 7800 F FEG-SEM) and atomic force microscopy (AFM, JPK Nanowizard 3 AFM-SKP) was used to study the surface topography of nickel oxide films. The surface chemistry of films was analysed by X-ray photoelectron spectroscopy (XPS, Kratos Axis Supra). The blocking effect of the nickel oxide layers was evaluated by cyclic voltammetry (CV) with a Gamry 600 potentiostat using a non-aqueous electrolyte containing 2 mM ferrocene ($Fe(C_5H_5)_2$) and 0.1 M solution of tetrabutylammonium hexafluorophosphate ($Bu_4N^+PF_6^-$) in acetonitrile. The counter electrode was a platinum wire and Ag/Ag^+ electrode was used as a reference. All scan rates of CV measurements were performed at 50 mV/s. The resistance of the films was obtained from the slope of I-V curves for the FTO/NiOx/Ag structure. These I-V curves were measured with a Keithley 2400 source meter from 2 V to −0.1 V and from −0.1 V to 2 V, with a step size of 50 mV and a scan rate of 108 mV/s (due to the configuration of the equipment). For the photovoltaic characterisation of the perovskite devices, the current voltage curves of the devices were also measured with the above equipment and a class AAA solar simulator (Newport Oriel Sol3A), under simulated AM1.5 sun illumination (calibrated against a KG5 filtered silicon reference cell, Newport Oriel 91150-KG5). A mask of (0.09 $cm)^2$ was employed to avoid contributions from scattered light from the glass. The I-V curves were measured from 1.18 V to −0.1 V and from −0.1 V to 1.18 V, with a step size of 20 mV and a scan rate of 93 mV/s (due to the configuration of the equipment).

3. Results and discussion

3.1. Nickel hydroxide precursor and metalorganic compound

Precursor powder (P1) was synthetised by co-precipitation as described in the experimental section. XRD analysis (green line, Fig. 1a) shows peaks with d-spacings values of 2.69, 2.33, 1.56 and 1.49 Å that can be related with the (100), (101), (110) and (111) crystallographic planes (respectively) of β-nickel hydroxide (JCPDS No. 14–0117). The low intensity and broadness of the peaks suggest a small particle size or sub-domains or may indicate low crystallinity. Agglomerates of small particles with particle sizes < 100 nm are observed in the SEM image (Fig. 1c), confirming the small particle size indicated by the XRD data. No obvious $Ni(OH)_2$ platelets were seen by SEM which can be linked to the low peak intensity observed in XRD. The notable difference in the amplitude of the $Ni(OH)_2$ peaks may be related to a rapid formation of the precursor powder, a consequence of using a strong alkali (NaOH 10 M) as a precipitation agent and low supersaturation conditions during precipitation. This generates a disordered growth of nickel hydroxide resulting in different peak widths[49]. The XRD diffractogram of the precursor powder treated for 2 h at 270 ºC (P2, black, Fig. 1a) shows better-defined peaks with d-spacings values of 2.43, 2.09, 1.49, 1.27 and 1.22 Å that are consistent with the expected nickel oxide peaks (JCPDS NiO nº: 78–0643) and are related to planes (111), (200), (220), (311) and (222), respectively. The crystallite size obtained from Scherrer equation ($D = k\lambda/\beta \cos\theta$), where D is the size of the particle, K is the Scherrer's constant (0.94) and λ is the X-ray wavelength (1.5406 Å) for this powder ranges from 2.7 to 4.3 nm. No nanoparticles can be distinguished in SEM analysis for P2 (Fig. 1d). If the sintering temperature of precursor powder is increased up to 500 °C, an increase in particle size and crystallinity of nickel oxide particles can be detected in XRD analysis (Supporting Information, Fig. S1a)). Nanoparticles with sizes <25 nm are observed for P3 (SI, Fig. S1b).

The TGA/DSC analysis of P1 (Fig. 1b) shows 2 main stages of mass loss: firstly, between 50 and 175 ºC related to a dehydration process of the nickel precursor ($Ni(OH)_2.xH_2O \rightarrow Ni(OH)_2 + xH_2O$, endothermic peak around 90 ºC) and then between 220 and 330 ºC related to a nickel hydroxide dehydroxylation process ($Ni(OH)_2 \rightarrow NiO + H_2O$, endothermic peak around 275 ºC)[50]. The 2nd stage of mass loss confirms that the transition from nickel hydroxide to nickel oxide happens at the expected temperature, within the range of temperatures previously observed by other researchers (270–320 ºC)[14,15,29,45–47,50].

The precursor powder P1 was used to obtain the nickel hydroxide-monoethanolamine complex, M1 as per the experimental procedure. The TGA curve of (Fig. 2a) shows 4 regions of mass loss corresponding to 4 dTG peaks at 160 ºC, 195 ºC, 262 ºC and 390 ºC. The 1st and 2nd peaks can be related to the loss of MEA (53 % and 14.6 % mass loss with respect to the initial mass, respectively). The boiling point of MEA (170 ºC) is similar to the value of the first dTG peak observed, indicating that this evaporated MEA may not bonded to the nickel[51]. The second dTG peak appears at a temperature higher than the MEA boiling point (195 ºC vs 170 ºC) suggesting that this MEA is coordinated to the nickel hydroxide[51]. The 3rd peak can be related to the transition to nickel oxide [50]. The 4th loss of mass observed at 390 ºC and associated with a high intensity exothermic peak (Fig. 2a, DSC) is related to the elimination of the remaining carbonaceous residues through oxidation[52]. Generally, a temperature higher than the precursor decomposition temperature is needed to obtain an organic-free metal oxide film in sol-gel processes that use amines as stabilizers[25,43]. In Figs. 2b and 2c, the GC-MS data of evolved gases from M1 at 400 ºC and 500 ºC, respectively are shown. The peak with the largest area observed in both analyses is the MEA peak (retention time: 774.5 s and 773.8 s, respectively). This points out that a large part of MEA is not coordinated to nickel hydroxide as observed in TGA analysis (Fig. 2a). On the other hand, the other main peaks that appear in both GC-MS analyses are related to amine-based compounds (e.g., methenamine, N-methoxy or pyrazine). The presence of these peaks suggests that there is some chemical bonding between the nickel hydroxide and part of the added MEA. Fig. 2d shows the FT-IR spectra of

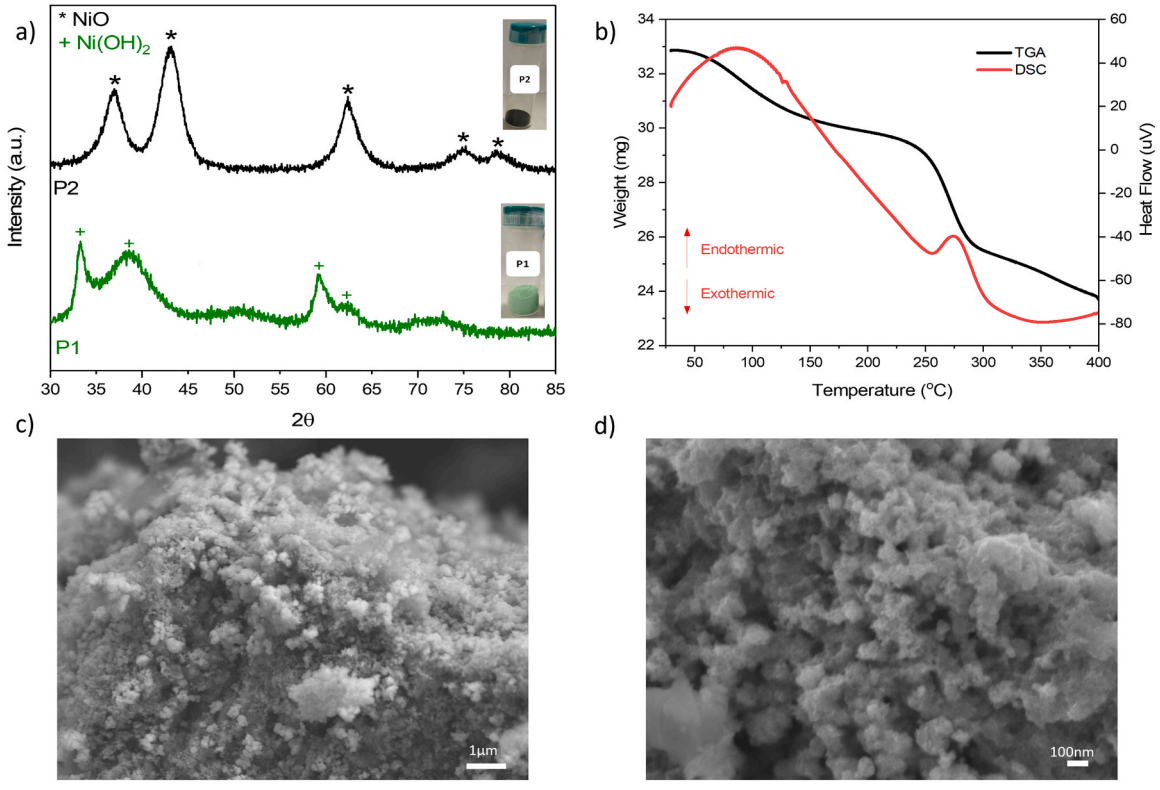

Fig. 1. a) XRD analysis of powders P1 (nickel hydroxide, precursor powder) and P2 (nickel oxide, sintered at 270 ºC for 2 h in a conventional oven), b) DSC/TGA nickel hydroxide precursor (P1),c) and d) SEM micrography of nickel hydroxide precursor powder (P1) and nickel oxide (P2).

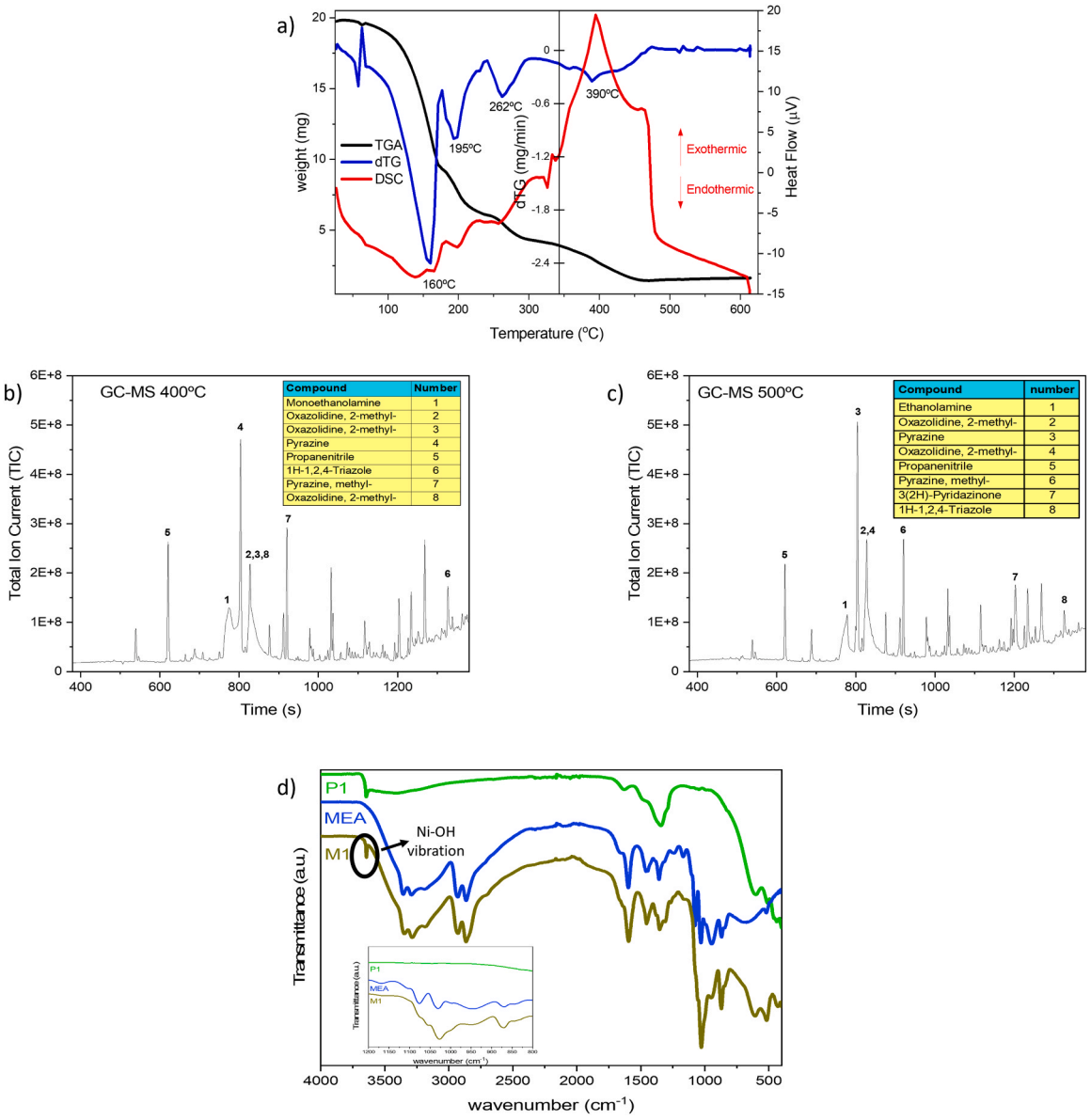

Fig. 2. a) DSC-TGA/dTG of M1 (nickel hydroxide powder and MEA mixture), b) GC-MS at 400 ºC of M1, c) GC-MS at 500 ºC of M1, d) FT-IR analysis of P1 (nickel hydroxide), MEA and M1(mixture of P1 and MEA).

P1, MEA and M1. The FT-IR spectrum of M1 shows a narrow and low-intensity peak around 3640 cm^{-1} related to $Ni(OH)_2$ (O-H stretching[53]). It also shows characteristic MEA peaks around 3400 and 3300 cm^{-1} (O-H and N-H stretching[54]) and 1600, 1360 and 1030 cm^{-1}. All the peaks mentioned above are shifted to lower wavenumber values with respect to the same peaks observed for P1 and MEA. The change in position of the characteristic bands of the MEA is normally caused by the interaction of the metal with the ligand system[55]. Lower wavenumber values are obtained when the molecular weight increases (since frequency of vibration is inversely proportional to the molecular weight of the vibrating molecule), which is consistent with the formation of a new chemical compound composed of ethanolamine and nickel hydroxide. Other characteristic MEA peaks around 1160, 1080, 950 cm^{-1} related to -C-C-, -C-N- or -C-O- stretching[54], greatly decreased in intensity or were not observed. This is commonplace when a ligand (MEA) coordinates with a metal (nickel)[55]. A new peak at 430 cm^{-1} related to the M-O bond (oxygen from MEA) also appears in the M1 spectrum[56]. These results confirm the formation of a metallic complex between nickel and MEA previously suggested by the GC-MS and DSC-TGA analyses.

3.2. Nickel oxide films

M1 was easily mixed with ethanol thanks to the excellent miscibility of MEA with polar organic solvents, thus obtaining particle dispersions (D samples).In Fig. 3a), it can be observed that the dispersion colour is different depending on the processing time −24 h, 48 h and 72 h- of the thermal treatment at 40 ºC (D_{24h}, D_{48h} and D_{72h} respectively). The colour change could be related with a partial oxidation of the starting Ni $(OH)_2$ (green) to NiOOH (black)[57].

These samples were deposited on bare glass via spin coating, thermally treated, and their transmittance measured using UV–vis spectroscopy (SI, Fig. S2). The average transmittance in the visible range (380–750 nm) of these samples is ≥86 %. The film transmission in the visible range is similar for the 3 samples. The dispersion with the shortest processing time should be selected (D_{24h}) to simplify the production of nickel oxide. However, to prepare NiO_x films, D_{48h} was used because D_{24h} showed incomplete dispersion of P1 (i.e., sediment at the

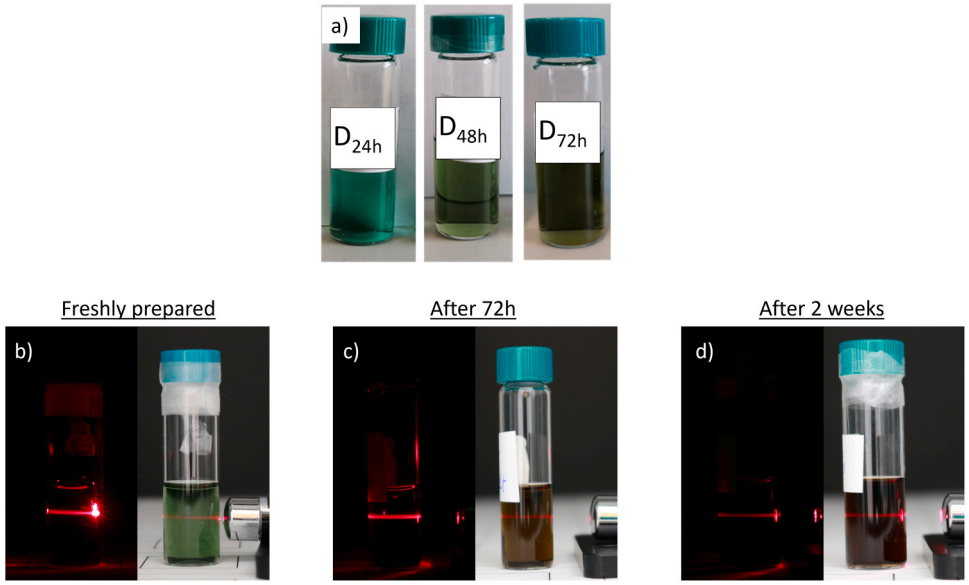

Fig. 3. a) Picture of 3 dispersions at 24 h, 48 h and 72 h of processing time at 40 ºC (hot-plate stirrer, ±5 °C) of M1, b) D_{48h} freshly prepared, c) D_{48h} 72 h after preparation, d) D_{48h} 2 weeks after preparation.

bottom of the vial after mixing with ethanol). A change in the colour of D_{48h} was observed over time (Fig. 3). This changed from bright green (freshly prepared sample) to yellowish brown at 72 h and dark brown at 2 weeks. This dark brown colour remains stable after 7 months of preparation (SI, Fig. S3). The Tyndall effect was observed when a red laser light (630–680 nm wavelength) passed through D_{48h} at these 3 stages of time (Fig. 3b), c) and d)) indicating the presence of suspended colloidal particles. Furthermore, no solid precipitation appeared after 7 months (SI, Fig. S3c)), confirming a stable colloidal dispersion. The colour change observed in Fig. 3b), c) and d) suggests again that nickel oxide is oxidised to nickel oxyhydroxide. FT-IR analysis of freshly prepared D_{48h} (green) and D_{48h} 72 h after preparation (brown-yellowish) showed the presence of a tiny peak at 3643 cm^{-1} (both) associated to Ni-OH vibration[58] (SI, Fig. S4, zoomed area). These peaks partially demonstrate that the nickel oxidation hypothesis is valid, since both Ni $(OH)_2$ and NiOOH show this band. However, we couldn't detect in D_{48h} (72 h) the presence of a band around 420 cm^{-1} related to Ni-O stretching vibration mode[58]. This band would have confirmed the presence of NiOOH but the band is probably too weak to be observed given that the higher intensity O-H stretch is only visible for this sample.

The spin-coated films prepared from D_{48h} were thermally treated for 30 min at different temperatures: 270 ºC (F_{270}), 320 ºC (F_{320}), 400 ºC (F_{400}) and 500 ºC (F_{500}). The transmittance spectra for these films are similar to bare FTO (Fig. 4). The samples processed at lower T (F_{270} and F_{320}) presented lower transmittance than FTO in some regions of the visible range (between 500 and 800 nm, Fig. 4, inset). F_{400} and F_{500} show a smaller difference in transmittance compared with FTO. The XRD analysis of these films (SI, Fig. S5) doesn't show any peaks related to nickel oxide or nickel hydroxide, since the FTO signal is very intense, and the expected NiO_x film thickness is very low.

The measurement of film resistance is presented in Fig. 5a. Samples F_{180} and F_{270} showed the highest (lowest gradient) and lowest (highest gradient) resistance, respectively. The large decrease in resistance from F_{180} to F_{270} is expected due to the transition from nickel hydroxide (very low conductivity) to NiO_x[59] at 270ºC. The oxide phase has better conductivity than the hydroxide, showing a greater difference in conductivity between both at temperatures close to 300 ºC[59]. On the other hand, from F_{270} to F_{320} the resistance increases and then decreases again with temperature (decreases from F_{320} to F_{400} and from F_{400} to F_{500}, Fig. 5a) so that F_{500} exhibits a similar film resistance to F_{270}. A different trend can be seen in the F-series contact angle measurements

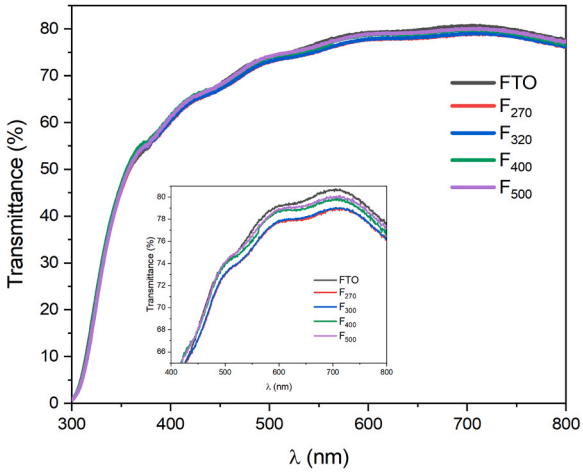

Fig. 4. Transmission spectra of D_{48h} films treated at different temperatures for 30 min (zoomed in transmittance range 65 %-81 %).

(Fig. 5b). The highest contact angles were observed for F_{180} (75.1º) and F_{400} (68.7º), respectively. The contact angle decreases several degrees when the temperature increases from 180 ºC (F_{180}, 73.6±1.5º) to 270 ºC (F_{270}, 55.9±2.8º). It remains similar at 320 ºC (F_{320}, 55.1±2.8º) and increases again at 400 ºC (F_{400}, 67.2±3.6º). Finally, the contact angle decreases again at 500 ºC (F_{500}, 55.7±1.9º) to reach values close to F_{270} and F_{320}. The film resistance and contact angle results suggest that surface modification is taking place during the thermal treatment. To further study changes in surface composition, XPS analysis was carried out (Fig. 5c and Fig. 5d) of the F-series. All F samples except F_{180} exhibit 2 peaks around 853.9 eV and 855.5 eV (Fig. 5c) that are characteristic of NiO and NiOOH contributing heavily to the composition. Nickel oxide exhibits a split spin-orbital with a difference between its components of 1.71 eV[60], which is similar to the that observed in all F samples but F_{180}. F_{180} only presents 1 peak at 856 eV (Fig. 5c), which is related to a majority presence of nickel hydroxide phases ($Ni2p_{3/2}$ $Ni(OH)_2$)[60]. The XPS data also confirm that the transition from nickel hydroxide to oxide has occurred at 270ºC. The O1s spectral component of nickel oxide is also found for samples F_{270}, F_{320}, F_{400} and F_{500} (peak around 529.3 eV [60], Fig. 5d).

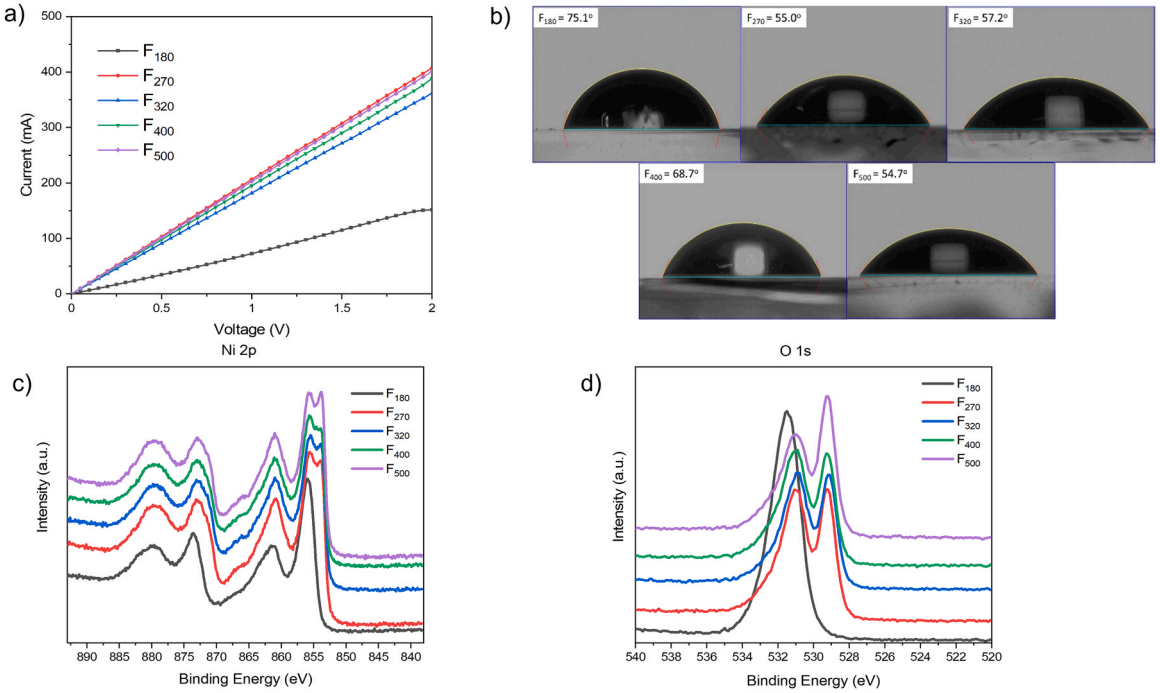

Fig. 5. a) Conductivity measurement of D_{48h} films treated at different temperatures (180, 270, 320, 400 and 500 °C) for 30 min, b) Contact angle measurements of D_{48h} films treated at different temperatures for 30 min, (representative angles were selected) c) Ni2p XPS measurements of F-series films, d) O1s XPS measurements of F-series films.

To clarify the compositional differences between these samples, a quantitative analysis of the spectra was carried out using the Biesinger *et al.* model[60,61]. Ni2p XPS signals related to $Ni(OH)_2$, NiOOH (β and γ) and NiO were considered for the quantification (SI, Fig. S6, example of phase deconvolution, F_{270}). The results showed (Table 2) that F_{180} contains negligible quantities of NiO (< 2 %). It initially increases to 63.1 % (F_{270}) to a maximum of 68.7 % (F_{500}), with the NiOOH phases decreasing from 29.6 % (F_{180}) to below 8 % for all other tested temperatures. It indicates a conversion from NiOOH + $Ni(OH)_2$ to NiO at 270 °C. Table 2 also shows that the lowest percentages of $Ni(OH)_2$ were obtained for F_{270} and F_{500} (29.4 % and 24.5 %, respectively). The amount of $Ni(OH)_2$ increased from 29.4 % (F_{270}) to 31.7 % and 34.4 % for F_{320} and F_{400}, respectively.

These values suggest that the higher contact angle obtained for F_{400} with respect to F_{270} can be related to a higher presence of nickel hydroxide. Whilst surprising, it has been demonstrated before that the hydroxide interacts weakly with water (hydrophobic) while other nickel species such as NiOOH[62] or nickel oxide[63] show a high affinity for it (hydrophilic). This weak interaction of $Ni(OH)_2$ with H_2O is observed in F_{180} with this sample showing the highest contact angle. The elimination of the remaining hydrophilic organics around 400 °C (confirmed by DSC/TGA analysis, Fig. 2a) would also explain the higher contact angle observed in F_{400}. As the temperature increases, the percentage of nickel hydroxide is expected to decrease as the amount of nickel oxide increases due to dehydroxylation[50]. This is clearly seen comparing F_{270} and F_{500} as $Ni(OH)_2$ decreases from 29.4 % to 24.5 % and NiO increases from 63.1 % to 68.7 % (Table 2). However, an unexpected increase in the amount of nickel hydroxide is observed for F_{320} and F_{400} with respect to F_{270} (Table 2). This is ascribed to the nickel-attached MEA disappearing from the film and reacting with some of the NiO present converting it into $Ni(OH)_2$ and NiOOH. The possible reaction stages could be as shown below:

Table 2
Percentage of each nickel specie obtained by XPS spectra deconvolution.

	NiO (%)	$Ni(OH)_2$ (%)	NiOOH (%)	Total (%)
F_{180}	1.5	68.9	29.6	100
F_{270}	63.1	29.4	7.5	100
F_{320}	63.2	31.7	5.1	100
F_{400}	57.9	34.3	7.8	100
F_{500}	68.7	24.5	6.8	100

1. $Ni(OH)_2NiOOH(MEA)_x + \quad MEA\left(free\right) \xrightarrow{270^{\circ}C} NiO_x(MEA)_y + A\ Ni(OH)_2 + D\ NiOOH + MEA(g)\Big) + OOC(g)\Big)$
2. $NiO_x(MEA)_y + \quad A\ Ni(OH)_2 + \quad D\ NiOOH \xrightarrow{400^{\circ}C} NiO_x(MEA)_z + BNi(OH)_2 + E\ NiOOH + OOC(g)$
3. $NiO_x(MEA)_z + B\ Ni(OH)_2 + E\ NiOOH \xrightarrow{500^{\circ}C} NiO_x + CNi(OH)_2 + F\ NiOOH + OOC(g)$

* $(MEA)_x > (MEA)_y > (MEA)_z$, $A < B$, $B > C$ and $A > C$, $D < E$, $E > F$ and $D > F$

** *OOC: Other Organic Compounds that are not MEA*

*** *NiO_x contains Ni^{+2} and Ni^{+3} species in an unknown ratio*

At 270°C, the nickel hydroxide metallic complex transitions to nickel oxide and, part of the MEA evaporates. Unbound MEA evaporates completely (2nd dTG peak in Fig. 2a) while the bonded MEA only partially evaporates (reaction 1). As the temperature increases, the MEA bond to NiO_x is broken, consequently producing a reverse transition from NiO_x to $Ni(OH)_2$ and NiOOH (reaction 2). The hypothesis of a reaction between MEA and nickel oxide that would generate more nickel hydroxides and new organic compounds is supported by the high presence of new amine-based compounds (e.g., pyrazine or triazole) detected in GC-MS analyses (Figs. 2b and 2c). The organic matter bonded to nickel completely disappears around 450 °C (end of mass loss, DSC-TGA analysis, Fig. 2a). Above 450 °C, no presence of organic matter is detected, which means that no extra $Ni(OH)_2$ should be generated (no reverse transition from oxide to hydroxide happening from this temperature). The remaining nickel hydroxide is then easily dehydroxylated at 500 °C (reaction 3), which explains the high increase in the amount of

NiO observed in F_{500} with respect to F_{400} (Table 2). These reactions were simplified by not adding possible by-products such as $Ni(OH)_2$(MEA) or NiOOH(MEA). This makes the reactions easier to understand and keeps the focus on NiO_x, $Ni(OH)_2$ and the NiOOH interaction. The high number of compounds taking part in these proposed reactions, very clearly shows the complexity of producing nickel oxide electrodes which is why they are difficult to make consistently to a high quality.

On the other hand, the difference in the resistance of the films can be explained by the presence of different species of nickel and organic matter and the size of NiO_x crystals. Samples F_{180} and F_{270} showed the highest and lowest film resistance, respectively (Fig. 5a) in the F-series. This agrees with Wu and Hsieh observations[64]; before the transition to NiO_x, the hydroxides precursor shows a low conductivity that highly increases when the conversion to oxide happens and then decrease as the temperature increases. This important increase in conductivity (or decrease in resistance) due to the dehydroxylation is observed in F_{270} (mostly composed of NiO_x) when compared to F_{180} (mostly composed of nickel hydroxides). The conductivity then decreases with temperature, perhaps due to the increase in the grain size[64]. The increase in resistance from the NiO_x formation (in our case at 270ºC) can be observed in sample F_{320} which shows a higher resistance than F_{270} (Fig. 5a). Its higher resistance may also be associated with the higher presence of $Ni(OH)_2$ (non-conductive) and lower presence of NiOOH (conductive) with respect to F_{270} (Table 2). However, F_{400} showed lower resistance than F_{320} even though it contains a higher percentage of Ni $(OH)_2$ and a possibly larger nickel oxide grain size[64].In this case, the lower resistance of F_{400} is related to the removal of non-conductive organic matter at 400 ºC (Fig. 2a, exothermic peak) and the increase of conductive Ni^{3+} compounds (NiOOH and NiO_x[33,65], Table 2) which increase charge carrying, p-type defects (holes) in the material. The decrease in resistance of sample F_{500} (Fig. 5a) is related to the large increase in conductive NiO_x phase and the decrease in $Ni(OH)_2$. The average RMS roughness for the FTO substrate, F_{270} and F_{500} is 37.23 nm, 25.84 nm and 52.67 nm, respectively (AFM measurements, SI, Fig. S7) which appears to be a reduction in substrate roughness for the F_{270} sample compared to the bare FTO indicating the peaks and troughs are evened out by the presence of the HTM layer. This may be beneficial in terms of electrical conductivity if this material is used in PSC devices[33, 66]. The apparent greater roughness of sample F_{500} compared to F_{270} is explained by the increase in grain size in F_{500} due to the higher temperature applied which may lead to a form of Ostwald ripening where smaller nanoparticles recystallise into larger ones.

Cyclic voltammetry is a simple and efficient method to explore the blocking effect on compact layers[67]. We used this method to compare the blocking effect of our NiO_x films (thin(270), thick(270), thin(500) and thick(500) samples) with control films (control(270) and control (500) samples). Both type of samples were sintered at 270 ºC and 500 ºC for 30 min. A description of the different samples prepared can be found in Table 1.

The CV data of pure FTO (Table 3) presents a Nernstian response, in which the peak-to-peak separation value (Δ_{EP}) between the anodic peak potential (E_{PA}) and the cathodic peak potential (E_{PC}) is 741 mV. Because of the signals detected, which are related to the redox reaction of ferrocene, bare FTO was proposed as the reference sample to evaluate the blocking performance of the NiO_x layers. The ratio of peak current density ($I_{P(NiOx)}/I_{P(FTO)}$ from the Randles-Sevcik equation[68]) could then be used to explain the electrochemical behaviour of the NiO_x layers.

$I_P = k \times n^{3/2} \times A \times c \times D^{1/2} \times \nu^{1/2}$ (Randles-Sevcik equation)[68]

* *k is a constant, n is the number of electrons transferred in the redox couple, A is the electrode area, D is the diffusion coefficient and ν is the scan rate.*

The blocking layer efficiency is higher if a lower $I_{P(NiOx)}/I_{P(FTO)}$ ratio is obtained. In our case the current density (I_P) value detected for the FTO substrate was the lowest among all the measured samples, making impossible to detect any blocking effect using the bare FTO as reference (Table 3). We also realised that the curves of the samples sintered at 270 ºC and 500 ºC were different (Fig. 6) and the I_P was higher for the high temperature samples (Table 3), which also holds true for bare FTO samples after a thermal treatment (SI, Fig. S8) indicating that the thermal process is impacting the substrate. Consequently, we can only compare samples sintered at the same temperature. It can be observed in Fig. 6a) and b) that CV curves are similar for our samples (nickel hydroxide precursor) and the control samples (nickel acetate precursor), showing the former ones lower I_P values than the latter ones (Table 3, e. g., 0.500 mA versus 0.529 mA, samples sintered at 500 ºC, B(500) and control(500), respectively). These lower values could indicate a better blocking effect for our nickel oxide samples or at least a similar blocking effect to that of the optimised control samples.

Table 3
Summary of CV characteristic of pure FTO and NiO_x thin films.

Samples	FTO	Thin (270)	Thick (270)	Control (270)	Thin (500)	Thick (500)	Control (500)
E_{PC} (mV)	805	635	651	637	581	579	577
E_{PA} (mV)	63	141	111	181	297	295	308
Δ_{EP} (mV)	741	494	540	456	284	283	269
I_{PC} (mA)	0.387	0.466	0.455	0.466	0.508	0.500	0.529

3.3. Performance in inverted perovskite solar cells

The NiO_x films thermally treated at 270 ºC and 500 ºC were used to fabricate inverted PSC devices. Both films, F_{270} and F_{500} showed the best wettability, electrical conductivity, and highest percentage of NiO_x among the prepared films. They also present a good morphology (AFM, SI, Fig. S7). Furthermore, films prepared at different thickness (6000 and 2000 rpm, thin and thick samples, respectively) have a similar CV performance than control samples. Hence both thicknesses and temperatures were studied with the aim of finding out how much it can influence the cell performance.

These results were below compared with those obtained for the control samples thermally treated at 270 ºC and 500 ºC.

The comparison between the mean values of J_{SC}, V_{OC}, FF and PCE of all samples was supported by a parametric statistical method, specifically a 2-sample unpaired t-test with a significance threshold for the two-tailed P value of 0.05 (5 %, Table S1). The normal distribution was verified with a Saphiro-Wilk test (Table S2) considering a significance level (α) of 0.05 (if P-value > α, the null hypothesis H_0 is accepted and therefore the data is assumed to be normally distributed).

3.3.1. Low-temperature sintered samples (270 ºC). Thin(270) and thick (270) vs control(270)

In Table 4, a higher mean FF is observed for the control samples sintered at 270 ºC compared to thin(270) and thick(270) samples. The result of the unpaired t-test showed that these mean differences between our samples and control samples are statistically significant (Table S1, forward and reverse measurements). It's suspected that the high differences between the FF of our samples and the control sample is related to the optimised thickness of control films, since no big differences in surface pinholes (current leaks) could be detected by CV analysis (Ip values 0.466, 0.455 and 0.466 mA for thin(270), thick(270) and control (270) respectively). Control sample presents a concentration of nickel oxide precursor (NiAc) of 0.20 M (Table 1) while our samples concentration is 0.11 M ($Ni(OH)_2$) meaning that thicker films have been probably obtained for the former. Remarkably, our thick(270) and thin (270) samples don't present statistically significant differences with the mean J_{SC} values of the control samples (Table S1), despite showing

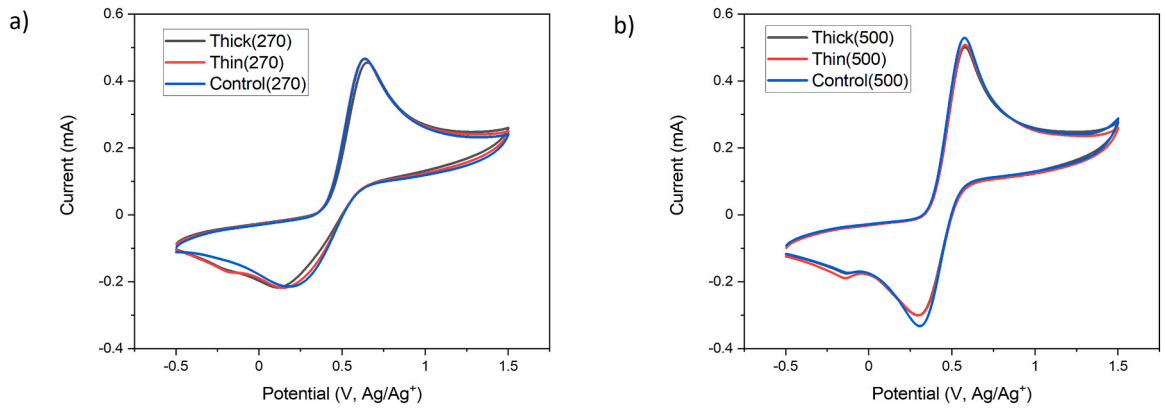

Fig. 6. - CV waves of bare FTO and NiO_x films prepared at different conditions a) thin(270), thick(270) and control(270) (270ºC) and b) thin(500), thick(500) and control(500) (500ºC).

Table 4
Electrical parameters on average ($\bar{X}$) and their standard deviation (σ) of thin(270), thin(500), thick(270), thick(500), control(270) and control(500) (18 pixels from 3 different devices measured).

	Jsc (mA/cm^2)				Voc (V)				FF (%)				Efficiency (%)			
	Voc to Jsc		Jsc to Voc		Voc to Jsc		Jsc to Voc		Voc to Jsc		Jsc to Voc		Voc to Jsc		Jsc to Voc	
	$\bar{X}$	σ	$\bar{X}$	σ	$\bar{X}$	σ	$\bar{X}$	σ	$\bar{X}$	σ	$\bar{X}$	σ	$\bar{X}$	σ	$\bar{X}$	σ
Thin(270)	15.9	1.8	15.9	1.9	1.00	0.04	0.99	0.01	64.0	9.2	68.0	9.5	10.1	1.7	10.7	1.6
Thin(500)	15.2	2.2	15.3	2.3	1.01	0.04	0.96	0.05	74.1	8.9	75.5	8.1	11.4	2.5	11.1	2.3
Thick(270)	16.1	1.5	16.1	1.6	1.00	0.03	0.99	0.01	68.3	8.6	71.4	8.5	11.1	2.3	11.5	2.2
Thick(500)	17.4	1.3	17.5	1.4	1.02	0.04	1.00	0.05	71.5	7.8	75.6	6.8	12.8	2.0	13.3	2.0
Control(270)	15.6	1.4	16.0	1.6	1.02	0.02	0.98	0.03	75.5	5.5	77.8	3.1	12.1	1.8	12.3	1.5
Control(500)	14.8	1.8	14.9	1.9	1.01	0.03	0.98	0.04	76.4	9.5	80.0	6.7	11.4	2.0	11.7	2.0

lower film transmittance (1.5 % less transmittance on average, Fig. S9, lower NiO_x transmittance means lower photons absorbed by perovskite) and using a solvent with lower boiling point (ethanol, 78ºC vs 2-methoxyethanol 125 ºC for control samples). Solvents with higher boiling point evaporate more slowly allowing the structural relaxation of the deposited film before its crystallisation, which favours the growth of aligned grains[51] giving a more homogeneous NiO_x surface. This would lead to a better crystallisation of the perovskite film and, consequently, to a higher short-circuit current[66]. Both factors are apparently not detrimental for our samples. These similar values of J_{SC} at lower thicknesses could be related to a higher presence (in percentage) of nickel oxide in our samples due to the use of a more suitable precursor (nickel hydroxide) at this sintering temperature (270 ºC). This would reduce the sheet resistance of our samples[69], which could allow more charges to be extracted from the perovskite absorber. The mean PCE difference between our thick(270) (non-optimised) and control(270) (optimised) cells (Table 4, 11.1 % versus 12.1 %, respectively) is also not statistically significant. This together with the current values obtained for these films and formulations with non-optimal parameters shows the potential of this new method to produce good NiO_x films at this temperature.

3.3.2. High-temperature sintered samples (500 ºC). Thin(500) and thick (500) vs control(500)

Thick(500) samples present the highest average efficiencies (Table 4) compared to thin(500) and control(500) samples. However, only control (500) samples present statistically significant differences with thick (500) in forward and reverse measurements (Table S1). The better PCE of thick(500) with respect to control(500) corresponds with a very statistically significant difference between their mean currents (Table S1). These lower J_{SC} values for control(500) samples could be related to the higher I_P (higher current leaking) observed by these samples (Table 3). Thin(500) samples showed a statistically significant improvement in their average FF over thin(270) samples (Table S1), which can be directly correlated with the higher presence of nickel oxide (XPS results, Table 2) and the elimination of the carbon residue (DSC/TGA, Fig. 2a) at 500 ºC.

However, control(500) didn't show a statistically significant improvement in any parameter with respect to the control samples prepared at low temperature (Table S1), although a decrease in the average J_{SC} and efficiency was observed (Table 4).

Thick(500) samples also provided the highest performance pixel (16.7 % versus 15.7 % of the control sample, Fig. S10) and, along with the highest average efficiencies, it shows the potential of this new method to produce quality NiO_x films that could be implemented as HTL on inverted PSCs with room for optimisation.

Finally, the electrical parameters of the devices built with our material at different thicknesses (samples thin and thick representing a spin-coating speed of 6000 and 2000 rpm, respectively) were compared to elucidate which factors could be responsible for better performance in our cells.

3.3.3. Comparison between films: Thin(270) and thin(500) vs thick(270) and thick(500)

Thin(270) and thick(270) don't show statistically significant differences in average J_{SC}, V_{OC}, FF and PCE, which could indicate similar surface compatibility with the perovskite.

Both samples sintered at 500 ºC (thin(500) and thick(500)) increase their average efficiency, although thick(500) is the only one that presents statistically significant differences with the samples sintered at 270 °C (Table S1). This is mainly due to a great improvement in J_{SC} (as mentioned in the previous comparison section). The increase in FF shown by 6000 rpm solar cells at 500 ºC (thin(500)) is noteworthy since it goes from 64.0 % and 68.0 % at 270 ºC to 74.1 % and 75.5 % (Table 4, V_{OC} to J_{SC} and J_{SC} to V_{OC} measurements, respectively). This difference is statistically significant according with Table S1. The increase in FF for thin(500) samples could be related to an improvement of the blocking

effect (BE) from 270 ºC to 500 ºC samples due to a higher film compactness obtained after the remaining carbon is removed (450 ºC, Fig. 2a). In terms of average J_{SC} and V_{OC}, thin(500) and thick(500) followed different paths when compared to samples of the same thickness sintered at lower temperature (thin(270) and thick(270), respectively). Thick(500) samples showed an average increase in both parameters with respect thick(270) (Fig. 7 and Table 4), but statistically significant differences were only detected in J_{SC}. V_{OC} values couldn't be compared statistically with the unpaired t-test since the set of V_{OC} values of thick(270) doesn't present a normal distribution (Table S2, reverse measurements). The same was observed for the V_{OC} values of thin(270) samples in forward and reverse measurements. On the other hand, thin (500) samples showed a decrease in average J_{SC} (Fig. 7 and Table 4) but it's not statistically significant (Table S1). The increase in RMS roughness observed in AFM analysis for thin(500) (52.67 for F_{500} = thin(500), 25.84 for F_{270} = thin(270)) could lead to a decrease in V_{OC} and J_{SC} since a rougher NiO_x film hinders the perovskite crystal formation and its film uniformity, resulting in lower J_{SC} and V_{OC}[33]. However, this wasn't observed perhaps thanks to the increase in the presence of nickel oxide at 500 °C (XPS, Table 2) which balanced the current and voltage values with respect to thin(270). The thick(500) samples present the best compatibility with the perovskite film and hence the best electric parameters among the samples prepared.

4. Conclusions

We have detailed a new method to produce nickel oxide films from a nickel hydroxide-based precursor at temperatures as low as 270 ºC. This method is simple and could solve some of the problems previously observed in sol-gel and nanoparticle methods, such as the high processing temperature and the high number of steps to obtain NiO_x films. These improvements could make industrial-scale processing of NiO_x feasible. We have also demonstrated the synthesis of a nickel hydroxide-ethanolamine complex that disperses very rapidly in ethanol, and which produces a very stable colloid. All this makes this material suitable for use in a one-step solution method rather than previous multi-step processes developed for nickel hydroxide. The characteristics of the prepared films show a good correlation between the surface composition with the wettability and conductivity of the nickel oxide films. These characteristics have also helped to understand the electrical parameters obtained for the built PSC devices, which showed average efficiencies of 11.5 % and 13.3 % (J_{SC} to V_{OC} measurements) with maximum efficiencies values of 14.7 % and 16.7 % (NiO_x sintered at 270 °C and 500 °C, respectively). The results obtained for these cells are promising. They are close to those of control cells with average efficiencies of 12.3 % and 11.7 % (J_{SC} to V_{OC} measurements) and highest pixel efficiencies of 15.4 % and 15.7 %, (NiO_x sintered at 270 °C and 500 °C, respectively) and don't present statistically significant differences at low temperature. With further optimisation in terms of nickel oxide film thickness, processing time or UVO treatment, among others, the electrical properties of the perovskite-based devices could improve.

CRediT authorship contribution statement

Peter J. Holliman: Writing – review & editing. **Matthew L. Davies:** Writing – review & editing. **Cecile Charbonneau:** Writing – review & editing. **Jenny Baker:** Writing – review & editing, Funding acquisition. **Rodrigo Garcia Rodriguez:** Writing – review & editing, Investigation. **Rafael Martí Valls:** Writing – review & editing, Writing – original draft, Visualization, Methodology, Investigation, Data curation,

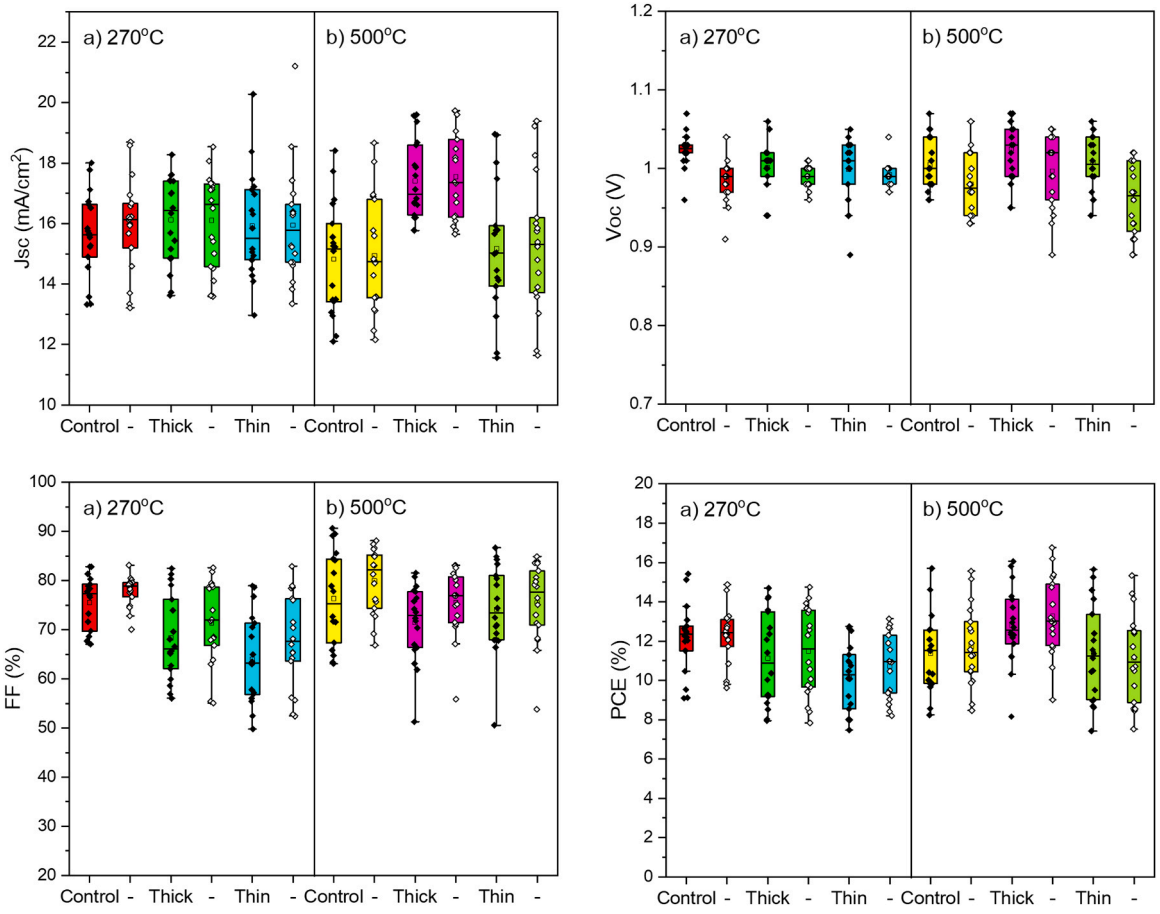

Fig. 7. Box plots of the electrical parameters of our samples (thin and thick) and control samples. Black circles reverse scan, white circles forward scan.

Conceptualization. **Tom Dunlop:** Investigation. **Diana Meza Rojas:** Writing – review & editing, Investigation. **Suzanne K. Thomas:** Investigation. **Eurig Jones:** Investigation.

Declaration of Competing Interest

The authors declare that they have no known competing financial interests or personal relationships that could have appeared to influence the work reported in this paper.

Data Availability

Data will be made available on request.

Acknowledgements

This research was funded by the 2014–2020 Structural Funds programme supporting the ERDF funded SPECIFIC 2 project and Engineering and Physical Sciences Research Council (EPSRC) through the SPECIFIC Innovation and Knowledge Centre (EP/N020863/1). We gratefully acknowledge funding from the EPSRC ECR Fellowship NoRESt EP/S03711X/1 (RMV and JB), EPSRC EP/P030068/1 (PJH), EP/S018107/1 (EWR) and the EU SPARC-II (DMR). RGR would like to acknowledge the IMPACT operation which has been part-funded by the European Regional Development Fund through the Welsh Government and Swansea University. The XPS, XRD and Raman systems were financed by Sêr Cymru Solar, a project funded by the Welsh Assembly Government. We would like to thank the access to characterisation equipment to Swansea University Advanced Imaging of Materials (AIM) facility, which was funded in part by the EPSRC (EP/M028267/1) and the European Regional Development Fund through the Welsh Government (80708).

Appendix A. Supporting information

Supplementary data associated with this article can be found in the online version at doi:10.1016/j.colsurfa.2024.134524.

References

[1] Y. Huang, H. Yang, T. Xiong, D. Adekoya, W. Qiu, Z. Wang, S. Zhang, M.-S. Balogun, Adsorption energy engineering of nickel oxide hybrid nanosheets for high areal capacity flexible lithium-ion batteries, Energy Storage Mater. 25 (2020) 41–51, https://doi.org/10.1016/j.ensm.2019.11.001.

[2] T.P. Mokoena, H.C. Swart, D.E. Motaung, A review on recent progress of p-type nickel oxide based gas sensors: Future perspectives, J. Alloy. Compd. 805 (2019) 267–294, https://doi.org/10.1016/j.jallcom.2019.06.329.

[3] S. Rakshit, S. Ghosh, S. Chall, S.S. Mati, S.P. Moulik, S.C. Bhattacharya, Controlled synthesis of spin glass nickel oxide nanoparticles and evaluation of their potential antimicrobial activity: A cost effective and eco friendly approach, RSC Adv. 3 (2013) 19348–19356, https://doi.org/10.1039/C3RA42628A.

[4] D.-L. Sun, B.-W. Zhao, J.-B. Liu, H. Wang, H. Yan, Application of nickel oxide nanoparticles in electrochromic materials, Ion. (Kiel.) 23 (2017) 1509–1515, https://doi.org/10.1007/s11581-017-1974-4.

[5] A. Singh, S.L.Y. Chang, R.K. Hocking, U. Bach, L. Spiccia, Highly active nickel oxide water oxidation catalysts deposited from molecular complexes, Energy Environ. Sci. 6 (2013) 579–586, https://doi.org/10.1039/C2EE23862D.

[6] A.M. Emara, E.S. Yousef, Structural and optical properties of phosphate-zinc-nickel oxide glasses for narrow band pass absorption filters, J. Mod. Opt. 65 (2018) 1839–1845, https://doi.org/10.1080/09500340.2018.1461942.

[7] S. Cui, Q. Wang, Y. Zhou, D. Mao, J. Bao, X. Song, Effect of nickel oxide and titanium oxide on the microstructural, optical, and mechanical properties of calcium hexaaluminate ceramics, Ceram. Int. 47 (2021) 35302–35311, https://doi.org/10.1016/j.ceramint.2021.09.073.

[8] V.K. Vyas, A.S. Kumar, S.P. Singh, R. Pyare, Destructive and non-destructive behavior of nickel oxide doped bioactive glass and glass-ceramic, J. Aust. Ceram. Soc. 53 (2017) 939–951, https://doi.org/10.1007/s41779-017-0110-2.

[9] A.M. Barros, D.C.R. Espinosa, J.A.S. Tenório, Effect of Cr2O3 and NiO additions on the phase transformations at high temperature in Portland cement, Cem. Concr. Res. 34 (2004) 1795–1801, https://doi.org/10.1016/j.cemconres.2004.01.016.

[10] M.P. Browne, H. Nolan, N.C. Berner, G.S. Duesberg, P.E. Colavita, M.E.G. Lyons, Electrochromic nickel oxide films for smart window applications, Int. J. Electrochem. Sci. 11 (2016) 6636–6647, https://doi.org/10.20964/2016.08.38.

[11] S. Sajid, A.M. Elseman, H. Huang, J. Ji, S. Dou, H. Jiang, X. Liu, D. Wei, P. Cui, M. Li, Breakthroughs in NiOx-HTMs towards stable, low-cost and efficient perovskite solar cells, Nano Energy 51 (2018) 408–424, https://doi.org/10.1016/j.nanoen.2018.06.082.

[12] S. Yue, K. Liu, R. Xu, M. Li, M. Azam, K. Ren, J. Liu, Y. Sun, Z. Wang, D. Cao, X. Yan, S. Qu, Y. Lei, Z. Wang, Efficacious engineering on charge extraction for realizing highly efficient perovskite solar cells, Energy Environ. Sci. 10 (2017) 2570–2578, https://doi.org/10.1039/C7EE02685D.

[13] J.J. Yoo, G. Seo, M.R. Chua, T.G. Park, Y. Lu, F. Rotermund, Y.-K. Kim, C.S. Moon, N.J. Jeon, J.-P. Correa-Baena, V. Bulović, S.S. Shin, M.G. Bawendi, J. Seo, Efficient perovskite solar cells via improved carrier management, Nature 590 (2021) 587–593, https://doi.org/10.1038/s41586-021-03285-w.

[14] K. Cao, Z. Zuo, J. Cui, Y. Shen, T. Moehl, S.M. Zakeeruddin, M. Grätzel, M. Wang, Efficient screen printed perovskite solar cells based on mesoscopic TiO2/Al2O3/NiO/carbon architecture, Nano Energy 17 (2015) 171–179, https://doi.org/10.1016/j.nanoen.2015.08.009.

[15] R. Li, P. Wang, B. Chen, X. Cui, Y. Ding, Y. Li, D. Zhang, Y. Zhao, X. Zhang, NiOx/spiro hole transport bilayers for stable perovskite solar cells with efficiency exceeding 21, ACS Energy Lett. 5 (2020) 79–86, https://doi.org/10.1021/acsenergylett.9b02112.

[16] J.R. Manders, S.-W. Tsang, M.J. Hartel, T.-H. Lai, S. Chen, C.M. Amb, J. R. Reynolds, F. So, Solution-processed nickel oxide hole transport layers in high efficiency polymer photovoltaic cells, Adv. Funct. Mater. 23 (2013) 2993–3001, https://doi.org/10.1002/adfm.201202269.

[17] A. Kanwat, W. Milne, J. Jang, Vertical phase separation of PSS in organic photovoltaics with a nickel oxide doped PEDOT: PSS interlayer, Sol. Energy Mater. Sol. Cells 132 (2015) 623–631, https://doi.org/10.1016/j.solmat.2014.10.010.

[18] J. Kim, N. Park, J.S. Yun, S. Huang, M.A. Green, A.W.Y. Ho-Baillie, An effective method of predicting perovskite solar cell lifetime–Case study on planar CH3NH3PbI3 and HC(NH2)2PbI3 perovskite solar cells and hole transfer materials of spiro-OMeTAD and PTAA, Sol. Energy Mater. Sol. Cells 162 (2017) 41–46, https://doi.org/10.1016/j.solmat.2016.12.043.

[19] D. Zhao, M. Sexton, H.-Y. Park, G. Baure, J.C. Nino, F. So, High-efficiency solution-processed planar perovskite solar cells with a polymer hole transport layer, Adv. Energy Mater. 5 (2015) 1401855, https://doi.org/10.1002/aenm.201401855.

[20] D. Wang, N.K. Elumalai, M.A. Mahmud, M. Wright, M.B. Upama, K.H. Chan, C. Xu, F. Haque, G. Conibeer, A. Uddin, V2O5 -PEDOT: PSS bilayer as hole transport layer for highly efficient and stable perovskite solar cells, Org. Electron. 53 (2018) 66–73, https://doi.org/10.1016/j.orgel.2017.10.034.

[21] M. Lv, J. Zhu, Y. Huang, Y. Li, Z. Shao, Y. Xu, S. Dai, Colloidal CuInS2 quantum dots as inorganic hole-transporting material in perovskite solar cells, ACS Appl. Mater. Interfaces 7 (2015) 17482–17488, https://doi.org/10.1021/acsami.5b05104.

[22] A. Neha, D.M. Ibrahim, H. Alexander, P. Norman, S. Frank, Z.S. Mohammed, G. Michael, Perovskite solar cells with CuSCN hole extraction layers yield stabilized efficiencies greater than 20%, Science 358 (80) (2017) 768–771, https://doi.org/10.1126/science.aam5655.

[23] C. Zuo, L. Ding, Solution-processed Cu2O and CuO as hole transport materials for efficient perovskite solar cells, Small 11 (2015) 5528–5532, https://doi.org/10.1002/smll.201501330.

[24] J.-Y. Jeng, K.-C. Chen, T.-Y. Chiang, P.-Y. Lin, T.-D. Tsai, Y.-C. Chang, T.-F. Guo, P. Chen, T.-C. Wen, Y.-J. Hsu, Nickel oxide electrode interlayer in CH3NH3PbI3 perovskite/PCBM planar-heterojunction hybrid solar cells, Adv. Mater. 26 (2014) 4107–4113, https://doi.org/10.1002/adma.201306217.

[25] A.T. Gidey, D.-W. Kuo, A.D. Fenta, C.-T. Chen, C.-T. Chen, First conventional solution sol–gel-prepared nanoporous materials of nickel oxide for efficiency enhancing and stability extending MAPbI3 inverted perovskite solar cells, ACS Appl. Energy Mater. 4 (2021) 6486–6499, https://doi.org/10.1021/acsaem.1c00496.

[26] T. Abzieher, S. Moghadamzadeh, F. Schackmar, H. Eggers, F. Sutterlüti, A. Farooq, D. Kojda, K. Habicht, R. Schmager, A. Mertens, R. Azmi, L. Klohr, J.A. Schwenzer, M. Hetterich, U. Lemmer, B.S. Richards, M. Powalla, U.W. Paetzold, Electron-beam-evaporated nickel oxide hole transport layers for perovskite-based photovoltaics, Adv. Energy Mater. 9 (2019) 1802995, https://doi.org/10.1002/aenm.201802995.

[27] J.W. Jung, C.-C. Chueh, A.K.-Y. Jen, A. Low-Temperature, Solution-processable, Cu-doped nickel oxide hole-transporting layer via the combustion method for high-performance thin-film perovskite solar cells, Adv. Mater. 27 (2015) 7874–7880, https://doi.org/10.1002/adma.201503298.

[28] M.B. Islam, M. Yanagida, Y. Shirai, Y. Nabetani, K. Miyano, NiOx hole transport layer for perovskite solar cells with improved stability and reproducibility, ACS Omega 2 (2017) 2291–2299, https://doi.org/10.1021/acsomega.7b00538.

[29] P.-H. Lee, T.-T. Wu, C.-F. Li, D. Głowienka, Y.-H. Sun, Y.-T. Lin, H.-W. Yen, C.-G. Huang, Y. Galagan, Y.-C. Huang, W.-F. Su, Highly crystalline colloidal nickel oxide hole transport layer for low-temperature processable perovskite solar cell, Chem. Eng. J. 412 (2021) 128746, https://doi.org/10.1016/j.cej.2021.128746.

[30] D. Koushik, M. Jošt, A. Dučinskas, C. Burgess, V. Zardetto, C. Weijtens, M. A. Verheijen, W.M.M. Kessels, S. Albrecht, M. Creatore, Plasma-assisted atomic layer deposition of nickel oxide as hole transport layer for hybrid perovskite solar cells, J. Mater. Chem. C. 7 (2019) 12532–12543, https://doi.org/10.1039/C9TC04282B.

[31] X. Yin, J. Liu, J. Ma, C. Zhang, P. Chen, M. Que, Y. Yang, W. Que, C. Niu, J. Shao, Solvothermal derived crystalline NiOx nanoparticles for high performance

perovskite solar cells, J. Power Sources 329 (2016) 398–405, https://doi.org/10.1016/j.jpowsour.2016.08.102.
[32] Y.-H. Chiang, C.-K. Shih, A.-S. Sie, M.-H. Li, C.-C. Peng, P.-S. Shen, Y.-P. Wang, T.-F. Guo, P. Chen, Highly stable perovskite solar cells with all-inorganic selective contacts from microwave-synthesized oxide nanoparticles, J. Mater. Chem. A 5 (2017) 25485–25493, https://doi.org/10.1039/C7TA07775K.
[33] T. Wang, D. Ding, H. Zheng, X. Wang, J. Wang, H. Liu, W. Shen, Efficient inverted planar perovskite solar cells using ultraviolet/ozone-treated NiOx as the hole transport layer, Sol. RRL 3 (2019) 1900045, https://doi.org/10.1002/solr.201900045.
[34] D.S. Saranin, V.N. Mazov, L.O. Luchnikov, D.A. Lypenko, P.A. Gostishev, D. S. Muratov, D.A. Podgorny, D.M. Migunov, S.I. Didenko, M.N. Orlova, D. V. Kuznetsov, A.R. Tameev, A. Di Carlo, Tris(ethylene diamine) nickel acetate as a promising precursor for hole transport layer in planar structured perovskite solar cells, J. Mater. Chem. C. 6 (2018) 6179–6186, https://doi.org/10.1039/C8TC01169A.
[35] L. Hu, J. Peng, W. Wang, Z. Xia, J. Yuan, J. Lu, X. Huang, W. Ma, H. Song, W. Chen, Y.-B. Cheng, J. Tang, Sequential deposition of CH3NH3PbI3 on planar NiO film for efficient planar perovskite solar cells, ACS Photonics 1 (2014) 547–553, https://doi.org/10.1021/ph5000067.
[36] Y. Guo, X. Yin, W. Que, NiOx mesoporous films derived from Ni(OH)2 nanosheets for perovskite solar cells, J. Alloy. Compd. 722 (2017) 839–845, https://doi.org/10.1016/j.jallcom.2017.06.185.
[37] F. Schackmar, H. Eggers, M. Frericks, B.S. Richards, U. Lemmer, G. Hernandez-Sosa, U.W. Paetzold, Perovskite solar cells with all-inkjet-printed absorber and charge transport layers, Adv. Mater. Technol. 6 (2021) 2000271, https://doi.org/10.1002/admt.202000271.
[38] B. Xia, I.W. Lenggoro, K. Okuyama, Preparation of nickel powders by spray pyrolysis of nickel formate, J. Am. Ceram. Soc. 84 (2001) 1425–1432, https://doi.org/10.1111/j.1151-2916.2001.tb00855.x.
[39] A.N. Puzan, V.N. Baumer, D.V. Lisovytskiy, P.V. Mateychenko, Structure transformations in nickel oxalate dihydrate NiC2O4·2H2O and nickel formate dihydrate Ni(HCO2)2·2H2O during thermal decomposition, J. Solid State Chem. 266 (2018) 133–142, https://doi.org/10.1016/j.jssc.2018.07.005.
[40] J.C. De Jesus, I. González, A. Quevedo, T. Puerta, Thermal decomposition of nickel acetate tetrahydrate: an integrated study by TGA, QMS and XPS techniques, J. Mol. Catal. A Chem. 228 (2005) 283–291, https://doi.org/10.1016/j.molcata.2004.09.065.
[41] A.M. El-Mahalawy, Structural and optical characteristics of nickel bis (acetylacetonate) thin films as a buffer layer for optoelectronic applications, Mater. Sci. Semicond. Process. 100 (2019) 145–158, https://doi.org/10.1016/j.mssp.2019.05.008.
[42] D. Zhan, C. Cong, K. Diakite, Y. Tao, K. Zhang, Kinetics of thermal decomposition of nickel oxalate dihydrate in air, Thermochim. Acta 430 (2005) 101–105, https://doi.org/10.1016/j.tca.2005.01.029.
[43] R. García-Rodríguez, D. Ferdani, S. Pering, P.J. Baker, P.J. Cameron, Influence of bromide content on iodide migration in inverted MAPb(I1−xBrx)3 perovskite solar cells, J. Mater. Chem. A. 7 (2019) 22604–22614, https://doi.org/10.1039/C9TA08848B.
[44] C. Sima, C. Grigoriu, S. Antohe, Comparison of the dye-sensitized solar cells performances based on transparent conductive ITO and FTO, Thin Solid Films 519 (2010) 595–597, https://doi.org/10.1016/j.tsf.2010.07.002.
[45] Q. He, K. Yao, X. Wang, X. Xia, S. Leng, F. Li, Room-temperature and solution-processable Cu-doped nickel oxide nanoparticles for efficient hole-transport layers of flexible large-area perovskite solar cells, ACS Appl. Mater. Interfaces 9 (2017) 41887–41897, https://doi.org/10.1021/acsami.7b13621.
[46] K.-T. Lee, J.-Y. Jang, S.J. Park, S.A. Ok, H.J. Park, Incident-angle-controlled semitransparent colored perovskite solar cells with improved efficiency exploiting a multilayer dielectric mirror, Nanoscale 9 (2017) 13983–13989, https://doi.org/10.1039/C7NR04069E.
[47] X. Yin, P. Chen, M. Que, Y. Xing, W. Que, C. Niu, J. Shao, Highly efficient flexible perovskite solar cells using solution-derived NiOx hole contacts, ACS Nano 10 (2016) 3630–3636, https://doi.org/10.1021/acsnano.5b08135.
[48] F. Jiang, W.C.H. Choy, X. Li, D. Zhang, J. Cheng, Post-treatment-free solution-processed non-stoichiometric NiOx nanoparticles for efficient hole-transport layers of organic optoelectronic devices, Adv. Mater. 27 (2015) 2930–2937, https://doi.org/10.1002/adma.201405391.
[49] A. Vecoven, D.R. Rahman, A.W. Apblett, Green process for preparation of nickel hydroxide films and membranes, J. Mater. Eng. Perform. 29 (2020) 5602–5608, https://doi.org/10.1007/s11665-020-05100-5.
[50] V. Logvinenko, V. Bakovets, L. Trushnikova, Decomposition processes of nickel hydroxide, J. Therm. Anal. Calor. 107 (2012) 983–987, https://doi.org/10.1007/s10973-011-1689-0.
[51] A. Pimentel, S.H. Ferreira, D. Nunes, T. Calmeiro, R. Martins, E. Fortunato, Microwave synthesized ZnO nanorod arrays for UV sensors: a seed layer annealing temperature study, Mater 9 (2016), https://doi.org/10.3390/ma9040299.
[52] M. Epifani, E. Melissano, G. Pace, M. Schioppa, Precursors for the combustion synthesis of metal oxides from the sol–gel processing of metal complexes, J. Eur. Ceram. Soc. 27 (2007) 115–123, https://doi.org/10.1016/j.jeurceramsoc.2006.04.084.
[53] A. Al-Hajry, A. Umar, M. Vaseem, M.S. Al-Assiri, F. El-Tantawy, M. Bououdina, S. Al-Heniti, Y.-B. Hahn, Low-temperature growth and properties of flower-shaped β- Ni(OH)2 and NiO structures composed of thin nanosheets networks, Superlattices Micro 44 (2008) 216–222, https://doi.org/10.1016/j.spmi.2008.04.008.
[54] M. Shabanian, M. Hajibeygi, A. Raeisi, 2 - FTIR characterization of layered double hydroxides and modified layered double hydroxides, in: S. Thomas, S.B.N. Daniel (Eds.), Woodhead Publ. Ser. Compos. Sci. Eng., Woodhead Publishing, 2020, pp. 77–101, https://doi.org/10.1016/B978-0-08-101903-0.00002-7.
[55] J. Wang, G. Yang, C.-Q. Li, W.-G. Shi, S.-H. Wang, Novel dendrimer-based nickel catalyst: synthesis, characterization and performance in ethylene oligomerization, Chem. Pap. 68 (2014) 1532–1538, https://doi.org/10.2478/s11696-014-0603-1.
[56] D.A. Köse, H. Necefoğlu, Synthesis and characterization of bis(nicotinamide) m-hydroxybenzoate complexes of Co(II), Ni(II), Cu(II) and Zn(II), J. Therm. Anal. Calorim. 93 (2008) 509–514, https://doi.org/10.1007/s10973-007-8712-5.
[57] X.-Z. Fu, Y.-J. Zhu, Q.-C. Xu, J. Li, J.-H. Pan, J.-Q. Xu, J.-D. Lin, D.-W. Liao, Nickel oxyhydroxides with various oxidation states prepared by chemical oxidation of spherical β-Ni(OH)2, Solid State Ion. 178 (2007) 987–993, https://doi.org/10.1016/j.ssi.2007.04.011.
[58] M.M. Kashani Motlagh, A.A. Youzbashi, F. Hashemzadeh, L. Sabaghzadeh, Structural properties of nickel hydroxide/oxyhydroxide and oxide nanoparticles obtained by microwave-assisted oxidation technique, Powder Technol. 237 (2013) 562–568, https://doi.org/10.1016/j.powtec.2012.12.047.
[59] H. Duan, Z. Chen, N. Xu, S. Qiao, G. Chen, D. Li, W. Deng, F. Jiang, Non-stoichiometric NiOx nanocrystals for highly efficient electrocatalytic oxygen evolution reaction, J. Electroanal. Chem. 885 (2021) 114966, https://doi.org/10.1016/j.jelechem.2020.114966.
[60] M.C. Biesinger, B.P. Payne, L.W.M. Lau, A. Gerson, R.S.C. Smart, X-ray photoelectron spectroscopic chemical state quantification of mixed nickel metal, oxide and hydroxide systems, Surf. Interface Anal. 41 (2009) 324–332, https://doi.org/10.1002/sia.3026.
[61] M.C. Biesinger, B.P. Payne, A.P. Grosvenor, L.W.M. Lau, A.R. Gerson, R.S.C. Smart, Resolving surface chemical states in XPS analysis of first row transition metals, oxides and hydroxides: Cr, Mn, Fe, Co and Ni, Appl. Surf. Sci. 257 (2011) 2717–2730, https://doi.org/10.1016/j.apsusc.2010.10.051.
[62] M.J. Eslamibidgoli, A. Groß, M. Eikerling, Surface configuration and wettability of nickel(oxy)hydroxides: a first-principles investigation, Phys. Chem. Chem. Phys. 19 (2017) 22659–22669, https://doi.org/10.1039/C7CP03396F.
[63] H. Zhu, H. Zhang, X. Ni, Z. Shen, J. Lu, Fabrication of superhydrophilic surface on metallic nickel by sub-nanosecond laser-induced ablation, AIP Adv. 9 (2019) 85308, https://doi.org/10.1063/1.5111069.
[64] M.-S. Wu, H.-H. Hsieh, Nickel oxide/hydroxide nanoplatelets synthesized by chemical precipitation for electrochemical capacitors, Electrochim. Acta 53 (2008) 3427–3435, https://doi.org/10.1016/j.electacta.2007.12.005.
[65] A.L. Dicks, Fuel cells – molten carbonate fuel cells | Cathodes. Encyclopedia of Electrochemical Power Sources, Elsevier, Amsterdam, 2009, pp. 462–466, 10.1016/B978-044452745-5.00265-3.
[66] H. Park, R. Chaurasiya, B.H. Jeong, P. Sakthivel, H.J. Park, Nickel oxide for perovskite photovoltaic cells, Adv. Photonics Res. 2 (2021) 2000178, https://doi.org/10.1002/adpr.202000178.
[67] P. Wang, Z. Shao, M. Ulfa, T. Pauporté, Insights into the hole blocking layer effect on the perovskite solar cell performance and impedance response, J. Phys. Chem. C. 121 (2017) 9131–9141, https://doi.org/10.1021/acs.jpcc.7b00979.
[68] T.-S. Su, T.-Y. Hsieh, C.-Y. Hong, T.-C. Wei, Electrodeposited ultrathin TiO2 blocking layers for efficient perovskite solar cells, Sci. Rep. 5 (2015) 16098, https://doi.org/10.1038/srep16098.
[69] J. Kim, H.R. Lee, H.P. Kim, T. Lin, A. Kanwat, A.R. bin Mohd Yusoff, J. Jang, Effects of UV-ozone irradiation on copper doped nickel acetate and its applicability to perovskite solar cells, Nanoscale 8 (2016) 9284–9292, https://doi.org/10.1039/C6NR01308B.